

# Improving Active-power Transfer Capacity of Virtual Synchronous Generator in Weak Grid

Shuan Dong and Yu Christine Chen

Department of Electrical and Computer Engineering

The University of British Columbia

Vancouver, BC, Canada

Email: shuan@ece.ubc.ca, chen@ece.ubc.ca

**Abstract**—The virtual synchronous generator (VSG) is a power-electronic controller that mimics the dynamic behaviour of synchronous generators. It is a promising technology to enable integration of renewable energy conversion systems under weak-grid conditions. By providing virtual inertia, the VSG improves system stability. However, under weak-grid conditions, system stability may also be adversely affected by the VSG exceeding its active-power transfer capacity, leading to a phenomenon known as *voltage instability*. In this paper, we highlight this problem via simulations conducted for a microgrid test system. Then, we offer analytical justification for the mechanism and root cause of the observed voltage instability. We further propose two countermeasures to improve the active-power transfer capacity. The first is based on existing VSG capabilities so that no new components are needed in the controller, and the second requires additional components but enables full use of the VSG capacity.

## I. INTRODUCTION

To contend with tremendous growth in renewable energy integration, the modern power system faces numerous challenges with respect to power availability and quality [1]. These include notable reduction in system inertia because, unlike conventional turbine-based generators, inverter-interfaced renewable energy sources (RESs) have low or no inertia. One way to address this problem is to design the inverter power-electronic controller so that it emulates dynamics arising from synchronous generators (SGs) and in turn provides virtual inertia to the grid—a concept known as virtual synchronous generator (VSG) [2]–[12]. The VSG can also enable frequency- and voltage-droop control, which leads to grid-stability improvements. Moreover, unlike conventional control methods such as vector-current control, VSGs operate well under weak-grid conditions, which is ideal in the integration of RESs that are oftentimes geographically situated in remote areas with weak transmission links to urban load centres [13].

Owing to the many benefits that VSGs offer in renewable energy integration, various aspects of VSGs have been extensively studied and improved over the past decade [2]–[8]. For example, [2] increases the VSG control freedom such that the RES has freely adjustable damping, [3] equips the VSG with self-synchronization capability such that the RES achieves plug-and-play operation, and [4] limits the VSG output current during fault conditions and endows the RES with low-voltage

ride-through capability. Also, [5] and [6] improve the VSG transient stability and the VSG reactive-power sharing performance, respectively. Furthermore, to facilitate the renewable energy integration using VSGs, [7] proposed a VSG-based wind turbine controller, and [8] presents a VSG-based multi-terminal HVDC design that are able to integrate large-scale renewable energy conversion systems. For VSGs that are weakly connected to the rest of the grid, which is typically the case for remotely located RESs, [9] maintains a safe stability margin by reducing the controller bandwidth, [10] stabilizes the system by appending a supplementary nonlinear controller, and [11] improves the system stability by reducing the high-frequency amplification effect.

An aspect of the VSG that has not been thoroughly investigated in the literature is the active-power transfer capacity of VSG-controlled RESs operating under weak-grid conditions. If the actual active power delivered from the RES to the load centre exceeds the transfer capacity, the system would not converge to a viable power-flow solution, and this leads to so-called voltage instability [14]. Conventionally, voltage stability is often compromised by heavy loading conditions, and the impacts of grid voltage variations on the voltage stability has been studied in [12]. In our setting, however, loss of stability stems from greater VSG active-power output than that can be delivered to the rest of the system. This paper reveals an important cause of voltage instability in VSG-integrated power systems. Particularly, we provide analysis for the mechanism of voltage instability under weak-grid conditions. We further propose two countermeasures to improve VSG active-power transfer capacity: (i) activate the voltage-droop controller, which requires the VSG to provide more reactive-power output, and (ii) use additional reactive-power compensation devices, so as to enable full use of the VSG capacity. It is worth noting that though voltage droop control and reactive-power compensation have been extensively studied before, they have not been used to improve VSG active-power transfer capacity under weak-grid conditions.

The remainder of the paper is organized as follows. In Section II, we describe a VSG-connected microgrid test system and demonstrate the necessity of studying VSG active-power transfer capacity. Analysis is provided in Section III, based on which we develop methods to improve the active-power transfer capacity. In Section IV, we verify the effectiveness of

proposed solutions via numerical simulations. Section V offers concluding remarks and directions for future work.

## II. PRELIMINARIES

In this section, we first provide an overview of the VSG design. Thereafter, we introduce a microgrid test system, in which a VSG operates under weak-grid conditions since it is connected to the external grid via a long transmission line. Finally, using this system as an example, we show the necessity of studying the VSG active-power transfer capacity.

### A. Virtual Synchronous Generator

As shown in Fig. 1, the active- and reactive-power loops of the VSG regulate its active-power output  $P_t$  and reactive-power output  $Q_t$  by varying its rotor angle  $\theta_g$  and excitation flux  $\psi_f$ , respectively. Also, depending on the statuses of Switches 1 and 2, denoted by  $S_1$  and  $S_2$ , respectively, the VSG can achieve frequency- and voltage-droop controls ( $S_i = 1$  if Switch  $i$  is ON, and  $S_i = 0$  if Switch  $i$  is OFF,  $i = 1, 2$ ). Specifically, as shown in Fig. 1(b), the dynamics of the VSG reactive-power loop (RPL) in Fig. 1(b) is described by

$$K_g \frac{d\psi_f}{dt} = (Q_t^* - Q_{tf}) + S_2 \sqrt{\frac{2}{3}} D_q (U_t^* - U_{tf}), \quad (1)$$

where the coefficient  $K_g$  determines the RPL response speed,  $Q_t^*$  and  $U_t^*$ , respectively, denote the reference value of the VSG reactive-power output  $Q_t$  and output voltage magnitude  $U_t$ , and  $Q_{tf}$  and  $U_{tf}$ , respectively, represent the filtered signals of  $Q_t$  and  $U_t$ . In (1), the voltage droop coefficient  $D_q$  is tuned based on the required amount of variation in  $Q_t$  for certain change in  $U_t$ . In the remainder of paper, we omit the dynamics of the low-pass filters (LPFs) in Fig. 1 and assume that  $Q_{tf} \approx Q_t$  and  $U_{tf} \approx U_t$ . We note that neglecting their dynamics facilitates our analysis without loss of accuracy, since voltage stability, which limits the VSG active-power transfer capacity, acts on a slower time-scale and is usually analyzed via static models (e.g.,  $PV$  and  $QV$  curves, continuation power flow, modal analysis, etc.) that are independent of these dynamics [14].

As for the VSG active-power loop (APL) in Fig. 1(a), it emulates SG rotor dynamics described by

$$J_g \frac{d\omega_g}{dt} = \frac{P_t^*}{\omega_N} - T_{ef} - D_f \frac{d}{dt} \left( \frac{T_{ef}}{\psi_{ff}} \right) - S_1 D_p (\omega_g - \omega_g^*), \quad (2)$$

$$\frac{d\theta_g}{dt} = \omega_g, \quad (3)$$

where  $J_g$  denotes the inertia constant,  $P_t^*$  the active-power reference value,  $\omega_N$  the rated angular frequency, and  $T_{ef}$  the filtered signal of the VSG electromagnetic torque  $T_e$ . In (2), the terms  $D_f \frac{d}{dt} \left( \frac{T_{ef}}{\psi_{ff}} \right)$  and  $S_1 D_p (\omega_g - \omega_g^*)$ , respectively, represent the damping correction loop, which adjusts the APL damping ratio, and the switchable frequency-droop controller, which achieves primary frequency control.

As shown in Fig. 1, with the RPL output  $\psi_f$  as well as the rotating speed  $\omega_g$  and the rotor angle  $\theta_g$  from the APL, we obtain the VSG inner voltage  $e_g$  with the line-to-line RMS value  $E_g = \sqrt{3}/2 \omega_g \psi_f$ .

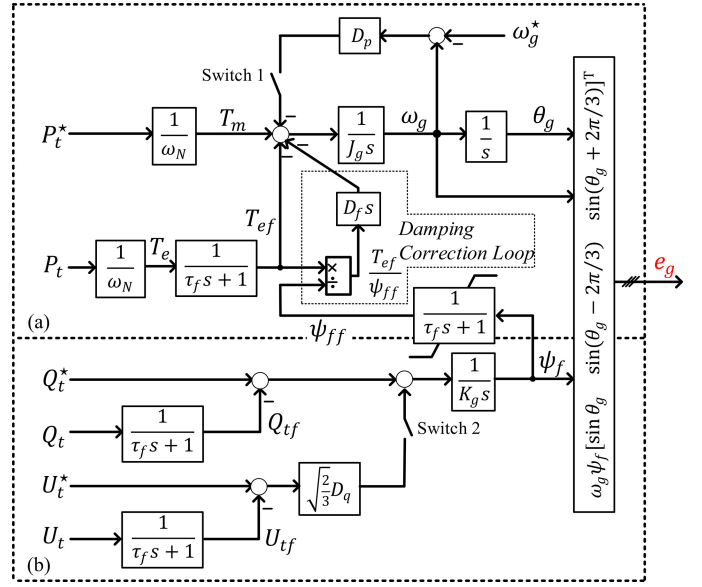


Fig. 1. Virtual synchronous generator augmented with damping correction loop [2]. (a) Active-power loop. (b) Reactive-power loop.

### B. Test System

Our aim is to study the active-power transfer capacity of the VSG under weak-grid conditions. In order to do so, we consider the microgrid test system shown in Fig. 2, where a VSG and two SGs (SG1 and SG2) provide power, behind three transformers, to three constant-impedance loads (Load1, Load2, and Load3). Furthermore, the VSG is connected to the rest of the system via a long transmission line (Line47). This setup is representative of the scenario in which VSG-interfaced devices (e.g., RESs and battery storage) must be located farther away from load centres due to geographical and

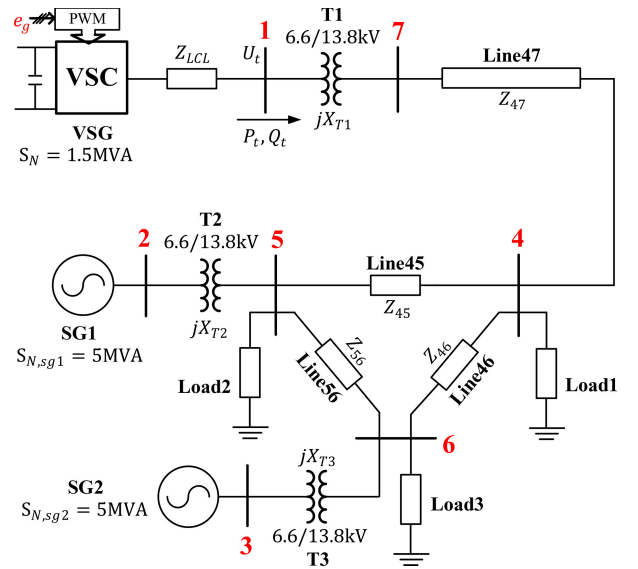


Fig. 2. Microgrid test system used to demonstrate the active-power transfer capacity of the virtual synchronous generator under weak-grid conditions.

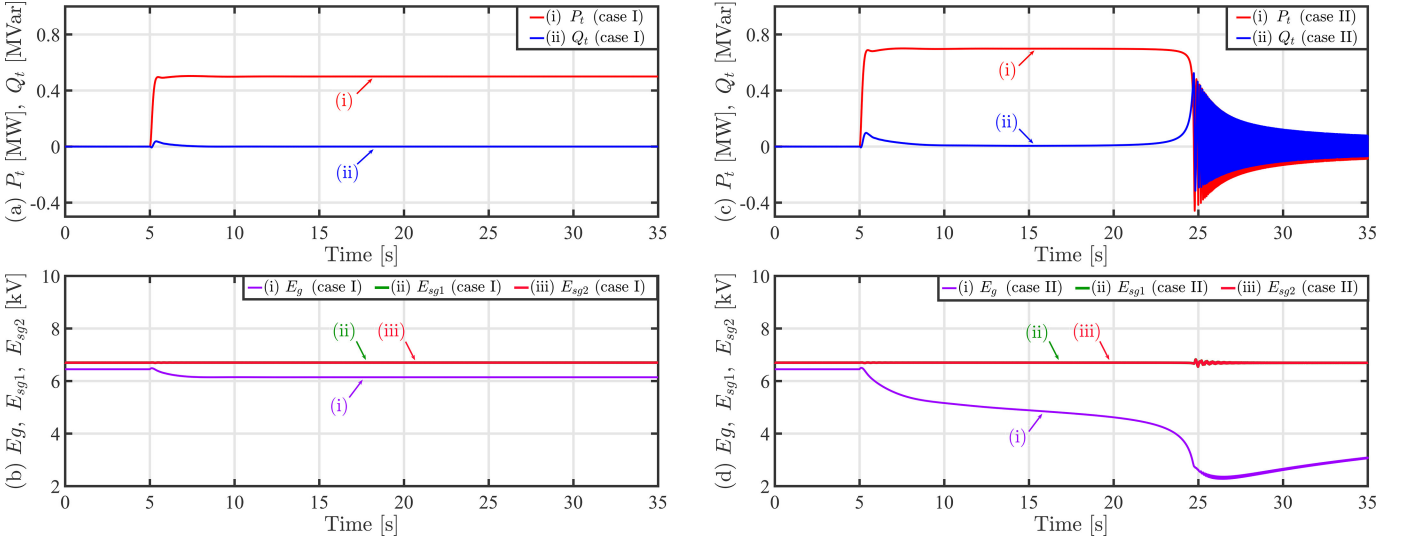


Fig. 3. Without voltage-droop controller: system dynamics caused by increasing the VSG active-power reference  $P_t^*$  from 0 to 0.5 (case I) and 0.7 MW (case II), respectively. (a)(b) Case I. (c)(d) Case II.

safety considerations. Note that to stabilize grid frequency and regulate grid voltage, both SGs are equipped with a modified Woodward governor (see Fig. 9) and a standard excitation controller (see Fig. 10). We refer readers to Appendices A–C for values used for VSG, SG, and network parameters.

### C. Problem Statement

With the the VSG controller and system described above, we motivate the necessity of studying the VSG active-power transfer capacity under weak-grid conditions via an example.

**Example 1 (Motivation).** In this example, we use the system in Fig. 2 to study the active-power transfer capacity of the VSG by increasing its active-power reference value  $P_t^*$  from 0 to 0.5 (case I) and 0.7 MW (case II) at  $t = 5.0$  s. In both cases, we set  $Q_t^*$  to be zero and deactivate frequency- and voltage-droop controls, which results in unity power factor and enables  $P_t$  ( $Q_t$ ) to track  $P_t^*$  ( $Q_t^*$ ) without steady-state error. In case I, as shown in Figs. 3(a), the VSG active-power output  $P_t$  (trace (i)) grows from 0 to 0.5 MW at  $t = 5.0$  s following the change in  $P_t^*$ . Also, as depicted in Fig. 3(b), the VSG inner voltage  $E_g$  (trace (i)) decreases from 6.5 to 6.1 kV and remains stable. On the other hand, as shown in Fig. 3(c), following the change in  $P_t^*$  from 0 to 0.7 MW, the VSG outputs initially converge to the desired setpoints but then begins to oscillate wildly about 20 s after the power-reference change. As shown in Fig. 3(d), the VSG inner voltage  $E_g$  gradually decreases beginning from  $t = 5.0$  s and finally collapses at  $t = 24.0$  s. After this moment, as shown in Fig. 3(c),  $P_t$  and  $Q_t$  becomes oscillatory and they are unable to converge to desired  $P_t^*$  and  $Q_t^*$ . ■

Based on the observations made in Example 1, we are motivated to seek analytical justification for the oscillatory behaviour in Fig. 3(c) and further propose countermeasures to prevent it even for large active-power transfer.

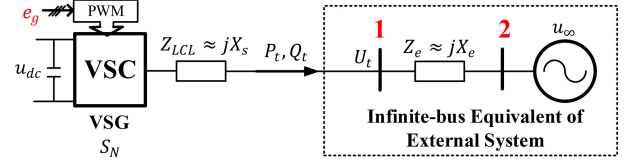


Fig. 4. Equivalent circuit of the system in Fig. 2 as seen from the VSG.

## III. VSG ACTIVE-POWER TRANSFER CAPACITY

In this section, we provide analytical justification for voltage instability due to violation of VSG active-power transfer capacity. Then based on the analysis, we propose countermeasures to improve the active-power transfer capacity of the VSG and avoid voltage instability in the system.

### A. Analysis of VSG Active-power Transfer Capacity

Our analysis of the VSG active-power transfer capacity begins with the derivation of an equivalent single-VSG infinite-bus system shown in Fig. 4, in which the infinite bus voltage is  $U_\infty = 6.8$  kV, the LCL filter impedance is  $Z_{LCL} \approx jX_s = j2.72 \Omega$ , and the equivalent impedance is  $Z_e \approx jX_e = j33.62 \Omega$  (we retain only the reactance  $X_e \gg X_s$ , since the network in Fig. 2 is assumed to be predominantly inductive). A full exposition of the derivation can be found in [15]. Let  $X_t$  denote the total system reactance, i.e.,  $X_t = X_s + X_e$ . Then the VSG active-power output  $P_t$  and reactive-power output  $Q_t$  can be expressed as, respectively,

$$P_t = \frac{E_g U_\infty \sin \theta_{g\infty}}{X_t}, \quad Q_t \approx \frac{E_g^2}{X_t} - \frac{E_g U_\infty \cos \theta_{g\infty}}{X_t}, \quad (4)$$

where  $U_\infty$  denotes the grid voltage, and  $\theta_{g\infty}$  denotes the phase-angle difference between  $E_g$  and  $U_\infty$ . By eliminating  $\theta_{g\infty}$  from (4), we get the following expression:

$$E_g^4 - (2X_t Q_t + U_\infty^2) E_g^2 + X_t^2 (P_t^2 + Q_t^2) = 0, \quad (5)$$

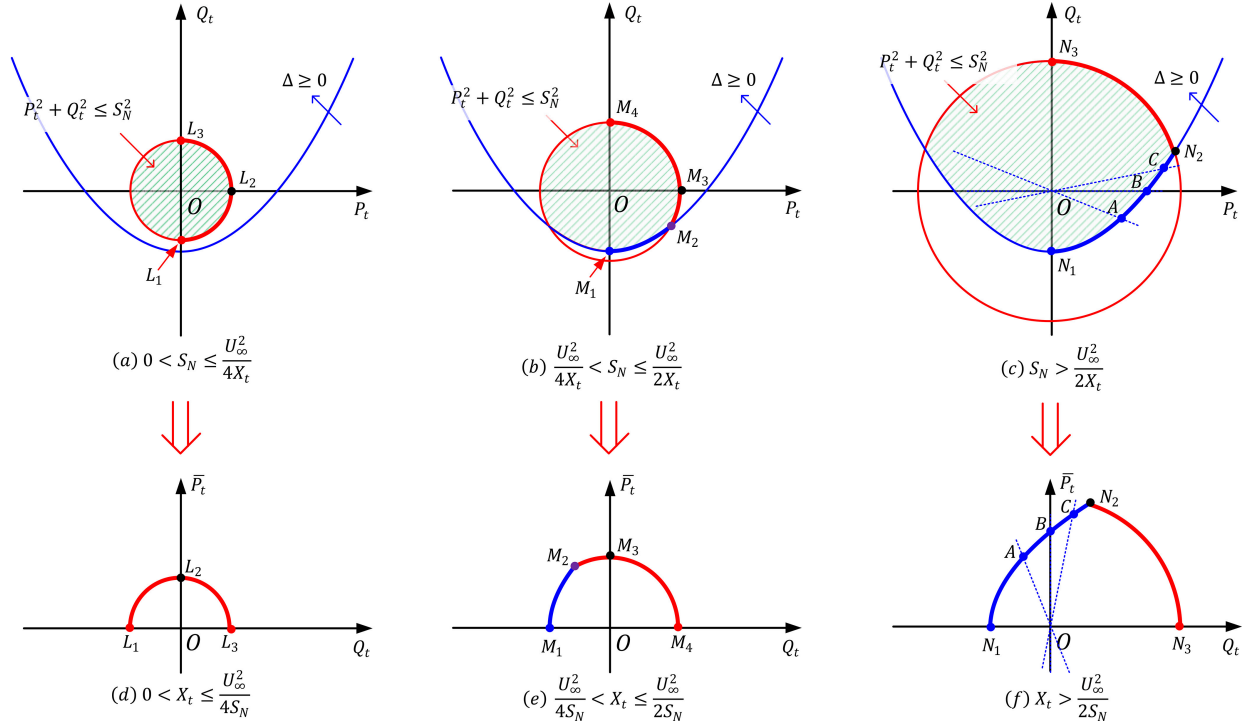


Fig. 5. VSG active-power transfer capacity  $\bar{P}_t(Q_t)$  for rated capacity  $S_N$  (grid impedance  $X_t$ ) in the ranges of (a)(d)  $0 < S_N \leq \frac{U_\infty^2}{4X_t}$  ( $0 < X_t \leq \frac{U_\infty^2}{4S_N}$ ), (b)(e)  $\frac{U_\infty^2}{4X_t} < S_N \leq \frac{U_\infty^2}{2X_t}$  ( $\frac{U_\infty^2}{4S_N} < X_t \leq \frac{U_\infty^2}{2S_N}$ ), and (c)(f)  $S_N > \frac{U_\infty^2}{2X_t}$  ( $X_t > \frac{U_\infty^2}{2S_N}$ ).

which is quadratic in  $E_g^2$ , and its discriminant is

$$\Delta = U_\infty^4 + 4X_t Q_t U_\infty^2 - 4X_t^2 P_t^2. \quad (6)$$

To ensure that the solution of (5) corresponds to a valid system operating point, the discriminant  $\Delta \geq 0$ , i.e.,

$$Q_t \geq \frac{X_t}{U_\infty^2} P_t^2 - \frac{U_\infty^2}{4X_t}. \quad (7)$$

Also, we bear in mind that due to the constraint of the VSG capacity  $S_N$ , the following condition should be satisfied:

$$P_t^2 + Q_t^2 \leq S_N^2. \quad (8)$$

Let  $\bar{P}_t(Q_t)$  denote the VSG active-power transfer capacity, which is the maximum value that  $P_t$  can take for a given value of reactive-power output  $Q_t$  within the space of feasible solutions delineated by (7) and (8). We plot this space in Fig. 5(a)–(c) for three different ranges of  $S_N$  in green hatched pattern, and we further mark  $\bar{P}_t(Q_t)$  in thick traces. Then, we focus on  $\bar{P}_t(Q_t)$  by flipping the  $P_t$ - and  $Q_t$ -axes in Figs. 5(a)–(c) to arrive at Figs. 5(d)–(f). Simultaneously, we reinterpret the conditions on  $S_N$  as ranges of values that the grid impedance  $X_t$  can take. Next, we derive closed-form expressions for  $\bar{P}_t(Q_t)$  in the three cases corresponding to Figs. 5(d)–(f). We will find the following functions useful:

$$f_1(Q_t) := \frac{U_\infty^2}{X_t} \sqrt{\frac{X_t}{U_\infty^2} Q_t + \frac{1}{4}} \geq 0, \quad (9)$$

$$f_2(Q_t) := \sqrt{S_N^2 - Q_t^2} \geq 0. \quad (10)$$

1)  $0 < X_t \leq \frac{U_\infty^2}{4S_N}$ : As shown in Fig. 5(d), we have

$$\bar{P}_t(Q_t) = f_2(Q_t), \text{ if } -S_N \leq Q_t \leq S_N. \quad (11)$$

As marked by  $L_2$  in Figs. 5(a) and (d),  $\bar{P}_t$  obtains its maximum value  $P_t^{\max} = S_N$  when  $Q_t = 0$ .

2)  $\frac{U_\infty^2}{4S_N} < X_t \leq \frac{U_\infty^2}{2S_N}$ : Corresponding to Fig. 5(e), we have

$$\bar{P}_t(Q_t) = \begin{cases} f_1(Q_t), & \text{if } -\frac{U_\infty^2}{4X_t} \leq Q_t \leq S_N - \frac{U_\infty^2}{2X_t}, \\ f_2(Q_t), & \text{if } S_N - \frac{U_\infty^2}{2X_t} < Q_t \leq S_N. \end{cases} \quad (12)$$

Similar to above,  $\bar{P}_t$  obtains its maximum value  $P_t^{\max} = S_N$  when  $Q_t = 0$ . This is marked by  $M_3$  in Figs. 5(b) and (e).

3)  $X_t > \frac{U_\infty^2}{2S_N}$ : As shown in Fig. 5(f), in this case,  $\bar{P}_t(Q_t)$  can also be expressed as (12). However, as marked by  $N_2$  in Figs. 5(c) and (f),  $\bar{P}_t$  reaches its maximum value

$$P_t^{\max} = \frac{U_\infty^2}{X_t} \sqrt{\frac{X_t S_N}{U_\infty^2} - \frac{1}{4}}, \quad (13)$$

when

$$Q_t = Q_t^{\max} = S_N - \frac{U_\infty^2}{2X_t} > 0. \quad (14)$$

**Example 2** (Explanation for Observations in Example 1). In this example, based on the analysis above, we provide analytical justification for the observations made in Example 1. Since the VSG in Fig. 2 operates under the weak-grid conditions

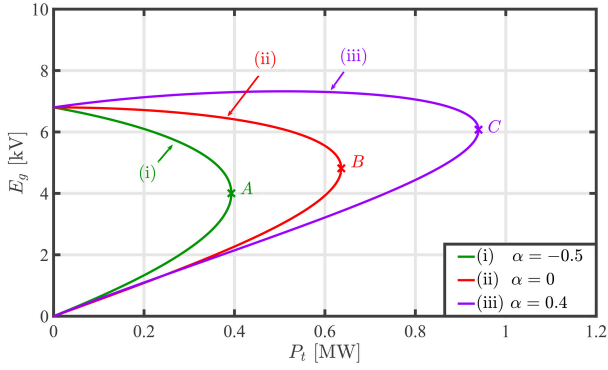


Fig. 6. VSG PV curves parameterized by  $\alpha$  with  $Q_t = \alpha P_t$ .

with large  $X_t = 36.34 \Omega > \frac{U_\infty^2}{2S_N} = 15.41 \Omega$  and its reactive-power output  $Q_t$  is regulated to zero, according to (12), the VSG active-power transfer capacity is  $\bar{P}_t(0) = 0.63$  MVA. Hence, in Example 1, case (I) with  $P_t = 0.5$  MW  $\leq \bar{P}_t(0)$  remains stable. On the other hand, case (II) with  $P_t = 0.7$  MW  $> \bar{P}_t(0)$  does not belong to the space of feasible solutions. Below, we further analyze the mechanism of the voltage instability in detail. ■

### B. Connection to Voltage Stability

If the VSG active-power output  $P_t$  exceeds  $\bar{P}_t(Q_t)$ , the so-called voltage instability will occur. Here, in order to reveal this, we assume that the VSG capacity  $S_N$  is sufficiently large so that it is not exceeded as  $P_t$  increases, i.e., the VSG active-power transfer capacity is located on the parabola between  $N_1$  and  $N_2$  in Figs. 5(c) and (f). Further define  $\alpha$  such that  $Q_t = \alpha P_t$ , which represents a straight line crossing the origin with slope  $\alpha$  in the  $P_t$ - $Q_t$  plane, as shown in Figs. 5(c) and (f). Then, we solve (5) for  $E_g$  as

$$E_g = \sqrt{\left(\frac{U_\infty^2}{2} + \alpha P_t X_t\right) \pm \frac{\sqrt{\Delta_\alpha}}{2}}, \quad (15)$$

where

$$\Delta_\alpha = U_\infty^4 + 4X_t \alpha P_t U_\infty^2 - 4X_t^2 P_t^2 \quad (16)$$

is the discriminant of (5) with  $Q_t = \alpha P_t$ . The expression in (15) describes the so-called PV curve (i.e., plot of  $E_g$  versus  $P_t$ ) parameterized by  $\alpha$ . Note that the introduction of  $\alpha$  enables us to study the influence of  $Q_t$  on the VSG active-power transfer capacity. The VSG PV curve has a “nose point” that represents the point of maximum possible active-power transfer capacity and the corresponding voltage. For a given  $\alpha$ , the nose point is located at

$$\bar{P}_t(\alpha) = \frac{U_\infty^2}{2X_t} \left( \alpha + \sqrt{\alpha^2 + 1} \right), \quad (17)$$

$$\bar{E}_g(\alpha) = \sqrt{\frac{U_\infty^2}{2} + \alpha P_t X_t}. \quad (18)$$

where  $\bar{P}_t(\alpha)$  is the solution to  $\Delta_\alpha = 0$ , and  $\bar{E}_g(\alpha)$  is obtained by setting  $\Delta_\alpha = 0$  in (15). According to (17),  $\bar{P}_t$  is inversely proportional to  $X_t$ , so the VSG active-power transfer capacity is limited with large  $X_t$ , i.e., under weak-grid conditions.

**Example 3** (Voltage Instability in Example 1). To further explain the observed voltage instability in Example 1, in Fig. 6, we plot the VSG PV curves for  $\alpha = -0.5, 0, 0.4$  and delineate their nose points as A, B, and C, respectively. These correspond to operating points marked with the same labels in Figs. 5(c) and (f). Particularly, if  $Q_t = 0$  (i.e.,  $\alpha = 0$ ), corresponding to the scenario in Example 1, trace (ii) in Fig. 6 reveals that the nose point B represents active-power transfer capacity  $\bar{P}_t = 0.64$  MW. This matches the observations made in Example 1, where the regulation of  $P_t$  to  $P_t^* = 0.7$  MW causes large oscillations in the output power. The increase in active-power output necessitates larger phase angle difference  $\theta_{g\infty}$  between the VSG and bus 2 in Fig. 4. However,  $Q_t$  also grows with larger  $\theta_{g\infty}$  (see (4) and trace (ii) in Figs. 3(a) and (c)), which is at odds with the second goal of regulating  $Q_t$  to  $Q_t^* = 0$ . Thus, the RPL resorts to decreasing the value of  $E_g$  in order to reduce the reactive-power output of the VSG (see Fig. 3(d)). This, in turn, reduces the active-power transfer capacity according to (4). If  $P_t^* < \bar{P}_t$  as in case I, the VSG finally converges to a point above the nose point on the PV curve. However, if  $P_t^* > \bar{P}_t$  as in case II, the system cannot converge to a viable power-flow solution, which leads to voltage instability. ■

### C. Improving VSG Active-power Transfer Capacity

Indeed, by comparing points A, B, and C in Fig. 5(f) or traces (i)–(iii) in Fig. 6, we find that with greater reactive-power output  $Q_t$ , or equivalently  $\alpha$ , the active-power transfer capacity  $\bar{P}_t$  of the VSG increases. We also see this by taking the derivative of  $\bar{P}_t(\alpha)$  in (17) with respect to  $\alpha$  and checking

$$\frac{d\bar{P}_t}{d\alpha} = \frac{U_\infty^2}{2X_t} \left( 1 + \frac{\alpha}{\sqrt{\alpha^2 + 1}} \right) > 0, \quad \forall \alpha \in \mathbb{R}. \quad (19)$$

Based on this, we propose to improve the VSG active-power transfer capacity by (i) activating voltage-droop control, and (ii) using reactive-power compensation.

1) *Voltage-droop Control*: According to (1), the voltage-droop controller allows the VSG to increase  $Q_t$  proportionally as  $U_t$  decreases (note that  $U_t \approx E_g$ ). This is evident by setting the derivative in (1) to zero to get

$$Q_t = Q_t^* + S_2 \sqrt{\frac{2}{3}} D_q (U_t^* - U_t). \quad (20)$$

With this in mind, we propose to enable the VSG voltage-droop controller in order to improve its active-power transfer capacity under weak-grid conditions. This is equivalent to increasing  $\alpha$  in Fig. 6, thus improving the VSG active-power transfer capacity. We note that the transfer capacity is also influenced by the values of parameters  $Q_t^*$ ,  $D_q$ , and  $U_t^*$ .

2) *Reactive-power Compensation*: Instead of the VSG itself, we can use reactive-power compensation devices, e.g., switched capacitors and static VAR compensators, to provide reactive power and improve the VSG active-power transfer capacity. For example, for our system in Fig. 2, we can install a switched capacitor  $C_w$  at bus 1 and provide more reactive power to maintain  $E_g$  at higher value. This method is also

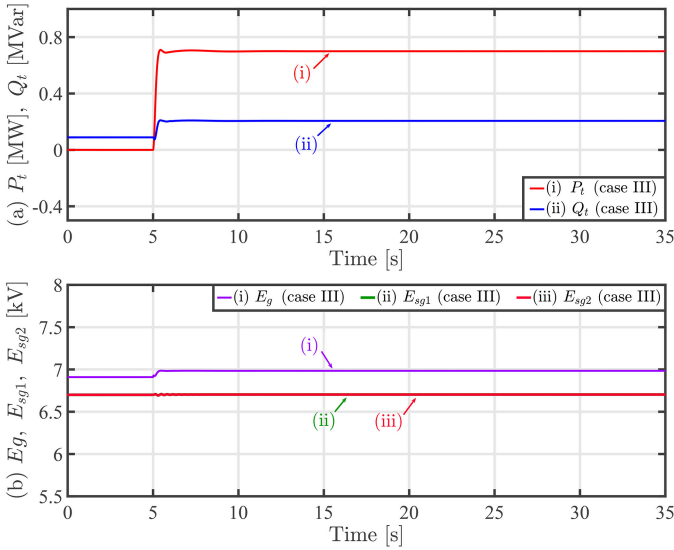


Fig. 7. With voltage-droop controller: system dynamics resulting from increasing the VSG active-power reference  $P_t^*$  from 0 to 0.7 MW.

equivalent to increasing  $\alpha$  in Fig. 6, and the additional reactive-power compensation devices allow us to make full use of the VSG capacity.

**Remark 1** (Trade-off of Increasing VSG Reactive Power). Above, we find that greater VSG reactive-power output increases its active-power transfer capacity. However, if the VSG reactive-power output is too high (e.g., see trace (iii) in Fig. 6), its output voltage remains close to the rated grid voltage value when its active-power output is about to reach the VSG active-power transfer capacity. In this case, the voltage instability is more difficult to predict, as it is not preceded by a significant voltage drop [14]. ■

#### IV. CASE STUDIES

In this section, via numerical simulations, we validate the effectiveness of the proposed methods to improve the VSG active-power transfer capacity. First, we show that activating voltage-droop control allows us to achieve so by increasing the VSG reactive-power output following increase in the active-power output. After that, we demonstrate that by adopting a switched capacitor, we can also support the VSG output voltage and increase its active-power transfer capacity. The simulated system is shown in Fig. 2, with parameter values reported in Appendices A–C, unless otherwise specified.

##### A. Activating Voltage-droop Control

In order to validate the efficacy of activating the voltage-droop controller, we close Switch 2 in Fig. 1, implement the reference signals from case II in Example 1, and plot resulting dynamics in Fig. 7. First, as shown by trace (i) in Fig. 7(a), we find that with the voltage-droop control in place, the VSG is able to inject  $P_t = 0.7$  MW into the grid, and system does not suffer from the oscillations that were observed in Example 1. This is because after sensing

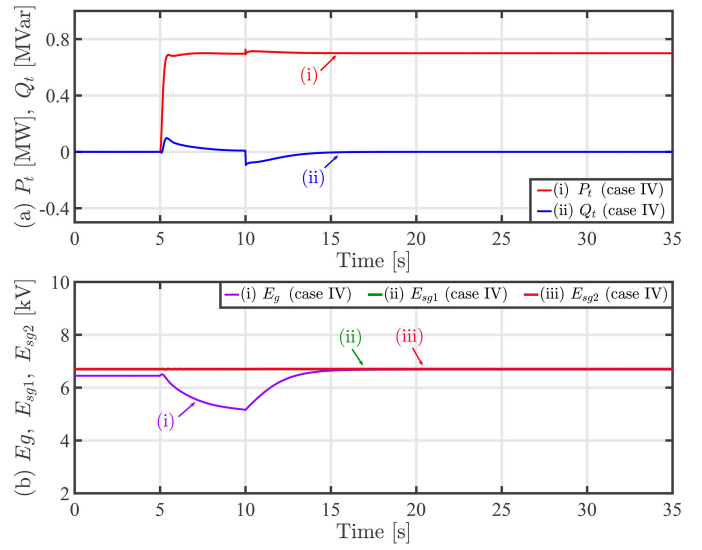


Fig. 8. With reactive-power compensation devices: system dynamics resulting from increasing the VSG active-power reference  $P_t^*$  from 0 to 0.7 MW.

the voltage drop caused by the increase in  $P_t$  at  $t = 5.0$  s, the voltage-droop controller enables the VSG to increase its reactive-power output from 0.09 to 0.20 MVar. This helps to maintain the VSG output voltage  $E_g$  (see trace (i) in Fig. 7(b)), operate the system above the nose point, and thus avoid the voltage collapse in Example 1.

##### B. Using Reactive-power Compensation Devices

After increasing  $P_t$  from 0 to 0.7 MW at  $t = 5.0$  s, we connect a fixed capacitor  $C_w = 10 \mu\text{F}$  to bus 1 at  $t = 10.0$  s. We note that the voltage-droop control is deactivated in this case. Simulation results are plotted in Fig. 8. The VSG output voltage  $E_g$  (trace (i) in Fig. 8(b)) drops following the increase of  $P_t$  (trace (i) in Fig. 8(a)) from 0 to 0.7 MW at  $t = 5.0$  s. Similar to case II in Example 1, this puts the system in danger of voltage instability. However, after connecting  $C_w$  at  $t = 10.0$  s,  $E_g$  is restored to a higher value, and as a result, the system avoids the voltage collapse observed in Example 1.

#### V. CONCLUDING REMARKS AND FUTURE WORK

In this paper, we motivate the necessity of studying VSG active-power transfer capacity under weak-grid conditions via a numerical example. We find that voltage stability is compromised if the maximum transfer capacity of the line connecting the VSG to the rest of the grid is exceeded. Then, we provide analytical justification for the VSG transfer capacity and determine the root cause of the observed voltage instability. Finally, based on our analysis, we propose two countermeasures to improve the VSG active-power transfer capacity and provide simulation verification.

Compelling avenues for future work include exploring other methods to improve VSG transfer capacity, comparing the voltage stability phenomena in traditional SG-based and modern power electronic-based power systems, and developing real-time voltage security assessment methods for future power grid with high penetration of VSG-based RESs.

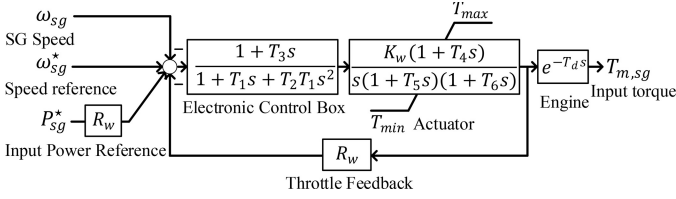


Fig. 9. Modified Woodward governor used in SG1 and SG2 to achieve primary frequency regulation [15].

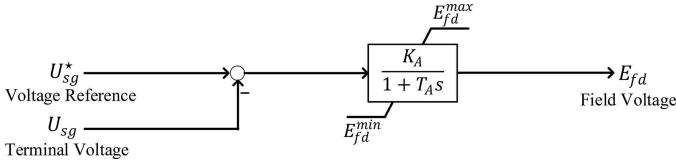


Fig. 10. Excitation system used in SG1 and SG2 to control their terminal voltages [16].

## APPENDIX

### A. Parameters of VSG System in Fig. 1

$S_1 = 0$ ,  $\tau_f = 0.01$  s,  $D_q = 7.42 \times 10^3$  Var/V,  $K_g = 5.60 \times 10^4$  Var · rad/V,  $\omega_g^* = \omega_N = 376.99$  rad/s,  $J_g = 28.7$  kg · m<sup>2</sup>,  $D_f = 2.13$  V · s<sup>2</sup>/rad.

### B. Parameters of SGs in Fig. 2

Generators SG1 and SG2:  $x_d = 1.56$  p.u.,  $x_q = 1.06$  p.u.,  $x'_d = x'_q = 0.296$  p.u.,  $x''_d = x''_q = 0.177$  p.u., inertia constant  $H_{sg} = 8.00$  s,  $T'_{d0} = 3.70$  s,  $T'_{q0} = 0.500$  s,  $T''_{d0} = T''_{q0} = 0.0500$  s, their rated frequency is 60 Hz, their rated voltage is 6.6 kV, and their rated capacity is 5 MW.

Modified Woodward governor used in SG1 and SG2 (see Fig. 9):  $\omega_{sg}^* = 1.00$  p.u.,  $P_{sg}^* = 1.00$  p.u.,  $K_w = 40.0$  p.u.,  $R_w = 0.0100$  p.u.,  $T_{max} = 1.10$  p.u.,  $T_{min} = 0.00$  p.u.,  $T_1 = 0.0100$  s,  $T_2 = 0.0200$  s,  $T_3 = 0.200$  s,  $T_4 = 0.250$  s,  $T_5 = 0.00900$  s,  $T_6 = 0.0384$  s, and  $T_d = 0.0240$  s.

Excitation system used in SG1 and SG2 (see Fig. 10):  $U_{sg}^* = 1.03$  p.u.,  $K_A = 140$ ,  $T_A = 0.0500$  s,  $E_{fd}^{max} = 6.00$  p.u., and  $E_{fd}^{min} = 0.00$  p.u.

### C. Parameters of Network in Fig. 2

Transformers T1, T2, and T3: turn ratio is 6.60/13.8 kV, rated frequency is 60 Hz, leakage reactance is 0.100 p.u., and rated capacities are, respectively, 1.5 MVA, 6.00 MVA, and 6.00 MVA.

Lines Line45, Line46, Line56, and Line47: rated frequency is 60 Hz, rated voltage is 13.8 kV, and impedances are, respectively,  $Z_{45} = 0.150 + j1.47 \Omega$ ,  $Z_{46} = 0.100 + j1.980 \Omega$ ,  $Z_{56} = 0.100 + j0.980 \Omega$ , and  $Z_{47} = 13.2 + j132 \Omega$ .

Constant-impedance Loads Load1, Load2, and Load3: rated frequency is 60 Hz, rated voltage is 13.8 kV, and impedances are, respectively,  $Z_{L1} = 61.0 + j12.2 \Omega$ ,  $Z_{L2} = 61.0 + j12.2 \Omega$ , and  $Z_{L3} = 46.9 + j5.86 \Omega$ .

## REFERENCES

- [1] B. Kroposki, B. Johnson, Y. Zhang, V. Gevorgian, P. Denholm, B.-M. Hodge, and B. Hannegan, "Achieving a 100% renewable grid: Operating electric power systems with extremely high levels of variable renewable energy," *IEEE Power and Energy Magazine*, vol. 15, no. 2, pp. 61–73, 2017.
- [2] S. Dong and Y. C. Chen, "Adjusting synchronverter dynamic response speed via damping correction loop," *IEEE Trans. Energy Convers.*, vol. 32, no. 2, pp. 608–619, Jun. 2017.
- [3] Q.-C. Zhong, P. L. Nguyen, Z. Ma, and W. Sheng, "Self-synchronized synchronverters: Inverters without a dedicated synchronization unit," *IEEE Trans. Power Electron.*, vol. 29, no. 2, pp. 617–630, Feb. 2014.
- [4] Z. Shuai, W. Huang, C. Shen, J. Ge, and Z. J. Shen, "Characteristics and restraining method of fast transient inrush fault currents in synchronverters," *IEEE Trans. Ind. Electron.*, vol. 64, no. 9, pp. 7487–7497, Sep. 2017.
- [5] L. Huang, H. Xin, Z. Wang, L. Zhang, K. Wu, and J. Hu, "Transient stability analysis and control design of droop-controlled voltage source converters considering current limitation," *IEEE Trans. Smart Grid*, vol. 10, no. 1, pp. 578–591, Jan. 2019.
- [6] H. Xu, X. Zhang, F. Liu, R. Shi, C. Yu, and R. Cao, "A reactive power sharing strategy of VSG based on virtual capacitor algorithm," *IEEE Trans. Ind. Electron.*, vol. 64, no. 9, pp. 7520–7531, Sep. 2017.
- [7] S. Wang, J. Hu, X. Yuan, and L. Sun, "On inertial dynamics of virtual-synchronous-controlled DFIG-based wind turbines," *IEEE Trans. Energy Convers.*, vol. 30, no. 4, pp. 1691–1702, Dec. 2015.
- [8] S. Dong, Y. Chi, and Y. Li, "Active voltage feedback control for hybrid multiterminal HVDC system adopting improved synchronverters," *IEEE Trans. Power Deliv.*, vol. 31, no. 2, pp. 445–455, Apr. 2016.
- [9] L. Zhang, L. Harnefors, and H. Nee, "Power-synchronization control of grid-connected voltage-source converters," *IEEE Trans. Power Syst.*, vol. 25, no. 2, pp. 809–820, May 2010.
- [10] M. Ashabani and Y. A. I. Mohamed, "Integrating VSCs to weak grids by nonlinear power damping controller with self-synchronization capability," *IEEE Trans. Power Syst.*, vol. 29, no. 2, pp. 805–814, Mar. 2014.
- [11] J. Fang, P. Lin, H. Li, Y. Yang, and Y. Tang, "An improved virtual inertia control for three-phase voltage source converters connected to a weak grid," *IEEE Trans. Power Electron.*, pp. 1–1, 2018.
- [12] J. Chen, T. O' Donnell, and F. Milano, "Assessment of grid-feeding converter voltage stability," *IEEE Trans. Power Syst.*, pp. 1–1, 2019, To be published.
- [13] L. Harnefors, M. Bongiorno, and S. Lundberg, "Input-admittance calculation and shaping for controlled voltage-source converters," *IEEE Trans. Ind. Electron.*, vol. 54, no. 6, pp. 3323–3334, Dec. 2007.
- [14] T. Van Cutsem and C. Vournas, *Voltage stability of electric power systems*. New York: Springer, 2005.
- [15] S. Dong and Y. C. Chen, "A method to directly compute synchronverter parameters for desired dynamic response," *IEEE Trans. Energy Convers.*, vol. 33, no. 2, pp. 814–825, Jun. 2018.
- [16] P. Sauer and M. Pai, *Power System Dynamics and Stability*. N.J.: Prentice Hall, 1998.